Supporting Information

Bipolar Conjugated Microporous Polymer with Intrinsically Fast Reaction Kinetics for High-Energy-Density and High-Rate-Capacity Symmetric All-Organic Lithium-Ion Battery

He Liu,[a] Likuan Teng,[a] Wesi He,[b] Xinzeyu Zhang,[a] Linchu Xu,[a] Ju Duan,[a] LuLu Wang,[a] Yumeng Zhang,[a] Bin Sun,[a] Yaozu Liao*[a] and Wei Lyu*[a]

a. State Key Laboratory of Advanced Fiber Materials, College of Materials Science and Engineering, Donghua University, Shanghai 201620, China.

b. College of Materials, Shanghai Dianji University, Shanghai, 201306, China

* Corresponding author. E-mail: wlyu@dhu.edu.cn; yzliao@dhu.edu.cn

Table of contents

S1. Experimental Methods

S1. 1. Materials

Tris (4–formylphenyl) amine (TA, 97%), 4,4',4"–(1,3,5–triazine–2,4,6–triyl) tribenzaldehyde (TT, 97%), and Ruthenium(III) chloride hydrate (98%) were purchased from Shanghai Haohong Biological Pharmaceutical Technology Co., Ltd. Pyrene (PT, 98%), acetonitrile (99%+), mesitylene (99%), N-Methylpyrrolidone (NMP) and Sodium periodate (99%+) were purchased from Shanghai Titan Scientific Co., Ltd; Dichloromethane (99.5%+), nitric acid, sulfuric acid (95~98.0%), $NaHCO_3$ (99%+), N,N–Dimethylformamide (DMF, 99.5%+), CS_2 (99%), N,N–Dimethylacetamide (DMAc, 98%+), acetic acid (99.5%+), tetrahydrofuran (THF, 98%+) were purchased from Sinopharm Chemical Reagent Co., Ltd. All chemical reagents were used as received without further purification.

S1. 2. Synthesis of Pyrene–4, 5, 9, 10–tetraone (PT)

PT was synthesized according to a previously reported method with slight modification.[1] Briefly, Pyrene (0.06 mol, 12.12g), dichloromethane (240 mL), acetonitrile (240 mL) and H_2O (300 mL) were added into a 1000 mL three–necked flask, stirred thoroughly to dissolve the solid completely. Ruthenium(III) chloride hydrate (1.26 mmol, 1.50 g) was then added and fully dissolved under continuous stirring. Then, the mixture was cooled to 0 ^oC in an ice water bath. Sodium periodate (0.49 mol, 105g) was added to the mixture over a period of 30 min, then the reaction mixture was stirred at 35–40 ^oC overnight. The reaction mixture was subjected to filtration to remove the solid residues, and the resulting filtrate was collected. The filtrate was washed with water several times, and an orange solid was obtained under vacuum. The, the crude product was washed with ethanol several times to afford PT: 12% yield. ^1H NMR (400 MHz, DMSO–d, δ ppm): 8.33 (d, Jm = 7.5 Hz, 4H)7.75 (t,H= 7.5 Hz,2H).

S1. 3. Synthesis of 2,7–Dinitropyrene–4,5,9,10–tetraone (PT–NO_2)

The PT–NO_2 was synthesized according to a previously reported method.[1] PT (4 mmol, 1.0 g) was added into a 40mL mixture of fuming nitric acid and sulfuric acid (1:4, v/v), and the mixture was heated to 90 ^oC for 4h. After cooling to room

temperature, the reaction mixture was poured into 400 mL cool water. The suspension was filtrated to obtain a yellow solid. The solid was neutralized with saturated $NaHCO_3$, and washed with water several times. The solid was dried under vacuum at 60 °C for 12h to afford PT–NO_2: 65% yield. ^{1}H NMR (400 MHz, DMSO–d, δ ppm): 8.89 (s, 4H).

S1. 4. **Synthesis of 2,7–Diaminopyrene–4,5,9,10–tetraone (PT–NH_2)**

The PT–NH_2 was synthesized according to a previously reported method.[1] PT–NO_2 (2.0 mmol, 704 mg) and $Na_2S{\cdot}9H_2O$ (24 mmol, 5.76 g) and N,N–Dimethylformamide (60 mL) were added to 100mL round–bottom. The mixture was stirred at 80 °C in N_2 atmosphere for 12 h. The solvent was removed by filtration, and the obtained solid was thoroughly washed in sequence with ethyl acetate, methanol, and water. After dried under vacuum at 60 °C for 12h, the as obtained PT–NH_2 was dispersed in 20 mL CS_2 and reflux at 50 °C for 15h. ^{1}H NMR (400 MHz, DMSO–d, δ ppm): 7.37 (s, 4H),5.96 (s, 4H).

S1. 5. **Synthesis of PTTA and PTTT**

PT–NH_2 (16.7 mg, 0.068 mmol), Tris (4–formylphenyl) amine (15 mg, 0.046 mmol), N,N–Dimethylacetamide (0.5 mL), mesitylene (0.5 mL) and 0.1 mL of 6 M aqueous acetic acid were added to a Pyrex tube. After sonication for 20 min, the Pyrex tube was quickly frozen by liquid N_2 followed by three freeze–pump–thaw cycles, and then the tube was sealed by flame. After recovered to room temperature, the tube was heated to 120 °C for 72 h. After the reaction tube cooled to room temperature, the crude product was collected through filtrate. The filtrated product was washed by THF, DMF, and acetone. Finally, the powder was dried at 100 °C under vacuum for 12 h to yield PTTA (22 mg, 68% yield). The synthesis process of PTTT was similar to that of PTTA, the different is the mass of PT–NH2 was 20 mg, the Tris (4–formylphenyl) amine was replaced by 4,4',4“–(1,3,5–triazine–2,4,6–triyl) tribenzaldehyde (15 mg). The mass of obtained PTTT was 30 mg, 91% yield.

S2. Characterization and measurements

S2. 1. Materials characterization

Fourier transform infrared spectra (FT-IR) were performed on a Nicolet 670 spectrometer. The Raman spectra were recorded on the Renishaw inVia-Reflex micro-Raman spectrometer, with the excitation light source being a 532 nm laser and the wavinem range being 650-2000 cm^{-1}. N_2 adsorption–desorption measurements were carried out on a Micromeritics ASAP 2460 surface area and porosity analyzer. Scanning electron microscope (SEM) images were acquired using a HITACHI Regulus 8230. ^{13}C solid-state NMR spectra were recorded on a Bruker Avance 400 spectrometer. The X-ray photoelectron spectra were performed on the Escalab 250Xi of Thermofisher. The X-ray diffraction (XRD) patterns were collected on Bruker D8 ADVANCE.

S2. 2. Electrochemical Measurements

Fabrication of coin-type half-cells: The active materials (PTTA or PTTT), Ketjen black and PVDF were thoroughly grinded and then NMP was added and configured into a uniform slurry. The resulting slurry was uniformly coated onto Cu foil or Al foil, followed by drying in a vacuum oven at 100 °C for 12 h. The dried electrodes were then punched into circular disks with a diameter of 12 mm as the working electrode, and the mass load of its active material was approximately 0.6 mg cm^{-2}. CR2032 coin cells were assembled by stacking the working electrode, a polypropylene (PP) separator, and lithium foil in sequence. A 1 M $LiPF_6$ solution in ethylene carbonate (EC) and ethyl methyl carbonate (EMC) (EC/EMC = 3:7, v/v) was used as the electrolyte. The galvanostatic charge–discharge (GCD) measurements were carried out on the NEWARE battery test instrument. The cathode was tested within a potential window of 1.5V to 4.3V, whereas the anode was tested within the potential window of 0.01 V to 3.0 V. The cyclic voltammetry (CV) and electrochemical impedance spectroscopy (EIS) were measured on electrochemical workstation (Interface 1000E, Gamry). The galvanostatic intermittent titration technique (GITT) measurements were carried out on a NEWARE battery testing system at a current density of 0.1 A g^{-1}, with each charge or discharge step lasting 10 min, followed by a relaxation period of 10 min.

Fabrication of coin-type SAOB: The electrodes were prepared using the same

method as that for half-cells. Using the same electrolyte system mentioned above, half-cells were first assembled to subject the cathode and anode to pretreatment: the cathode was charged to 4.3 V to achieve anion enrichment, while the anode was discharged to 0.01 V for pre-lithiation. This pretreatment aims to establish a potential difference between the electrodes and ensure a sufficient supply of lithium ions for the cathode. Post-pretreatment, the electrodes were disassembled from the half-cells and reassembled into CR2032 coin cells in the sequence of anode/separator/cathode with an appropriate volume of electrolyte. The assembled cells were rested for 5 h before use.

Fabrication of pouch-type SAOB: The assembly of pouch-type SAOBs follows the same principle as the coin cells: pre-treating the electrodes first, then sealing them with Al Laminate film. The main difference is the electrode preparation. A uniform slurry was coated onto a clean glass plate. Then, a piece of carbon cloth was placed on the coating for 1 min to absorb the slurry. The carbon cloth electrodes were dried in an oven at 60 ^{o}C and then in a vacuum oven at 100 ^{o}C. Carbon cloth was used here to increase the loading of active materials. Finally, the carbon cloth electrodes were attached to aluminum and copper foils, which served as the cathode and anode current collectors, respectively. Similar to the coin cells, the prepared cathode and anode were first assembled into half-pouch cells for pretreatment before being assembled into the final pouch-type SAOB.

S2. 3. Computational Details

All molecular geometry optimizations and energy calculations were performed using the Gaussian 16 software package.[2] Geometry optimizations and frequency calculations were carried out at the B3LYP/6-311G (d, p) level,[3, 4] with Grimme's D3 dispersion correction with Becke–Johnson damping (GD3BJ) applied to account for dispersion interactions.[5] The single point energies were computed at the B3LYP hybrid functional and def2-TZVP basis set.[6] Based on the above data, the binding energy was calculated from the following equation:

$$\Delta E = E_{PTTA-n\,ion} - E_{PTTA} - E_{n\,ion}$$

Where the $E_{PTTA-n\,ion}$, E_{PTTA}, and $E_{n\,ion}$ are the energy of ion (Li^+ or PF_6^-) adsorbed on the PTTA, the energy of PTTA and the energy of ion, respectively.

The HOMO, LUMO, ESP and IGMH were performed using the Multiwfn 3.8 [7] program and visualized with the VMD 1.9.3 package [8].

S2. 4. **Supplementary Equations**

Capacity Contribution Distribution

To quantitatively elucidate the kinetic characteristics of ion adsorption in the electrode material, the relationship between the peak current (i) and scan rate (v) was analyzed using the power-law equation:

$$i = av^b \quad \text{S1}$$

$$\log(i) = \log(a) + b\log(v) \quad \text{S2}$$

Here, a and b are constants, and the b-value provides insight to the relative contribution of pseudocapacitive behavior and diffusion-controlled process.

The capacitive- and diffusion-controlled contributions of samples were calculated by the following equation:

$$i = k_1v + k_2v^{1/2} \quad \text{S3}$$

where i and v represent the current response and scan rate, k_1 and k_2 are constant values.

Ions Diffusion Coefficient (D_{ions})

The galvanostatic intermittent titration technique (GITT) was performed on a Neware battery testing system at a current density of 0.1 A g-1, with a relaxation time of 10 min after each current pulse, to evaluate the ion diffusion coefficient (D_{ion}). The diffusion coefficient was calculated using the following equation:

$$D_{ion} = \frac{4}{\pi\tau}\left(\frac{m_B V_M}{M_B A}\right)^2\left(\frac{\Delta E_s}{\Delta E_\tau}\right)^2 \quad \text{S4}$$

Where m_B is the loading mass of active materials, V_M represents the molar volume of active materials, M_B is the molecular weight of active materials, A represent the area of the work electrode.

Theoretical capacity

The theoretical capacity of the electrode is related to the number of active sites in the material. The theoretical capacity can be calculated by the formula:

$$C_t = \frac{n \times F}{(3.6 \times M_w)} \quad \text{S5}$$

Where C_t is the theoretical capacity, F is Faraday constant (96485 C mol^{-1}), n represents the number of transferred electrons, and Mw is the relative molecular mass of the smallest energy storage unit. Based on the theoretical structure of a complete reaction (a stoichiometric ratio of 2:3, involving the condensation of 2 trialdehyde monomers with 3 diamine monomers and the elimination of 6 water molecules), the molecular weight (MW) is calculated to be 1427.45 for PTTA (2×329.35+3×292.25-6×18) and 1555.53 for PTTT (2×393.39+3×292.25-6×18). The electron transfer numbers for the cathode and anode are 20 and 102 for PTTA, and 26 and 124 for PTTT, respectively. The theoretical capacity of cathode C_{tc} is 375.6 mAh g^{-1}, and the theoretical capacity of anode C_{ta} is 1915.7 mAh g^{-1}. For PTTT, the C_{tc} is 448.0 mAh g^{-1}, C_{ta} is 1964.2 mAh g^{-1}.

Cathode-to-Anode Mass Ratio

The mass loading of the electrodes in the full cell needs to be adjusted according to the following equation:[9]

$$SC_A \times M_A \geq SC_C \times M_C \quad \text{S6}$$

where, SC_A is the anode specific capacity, SC_C is the cathode specific capacity, M_A is mass loading at the anode and M_C is the mass loading of the cathode.

S3. Supplementary Figures and Tables

S3. 1. Figures

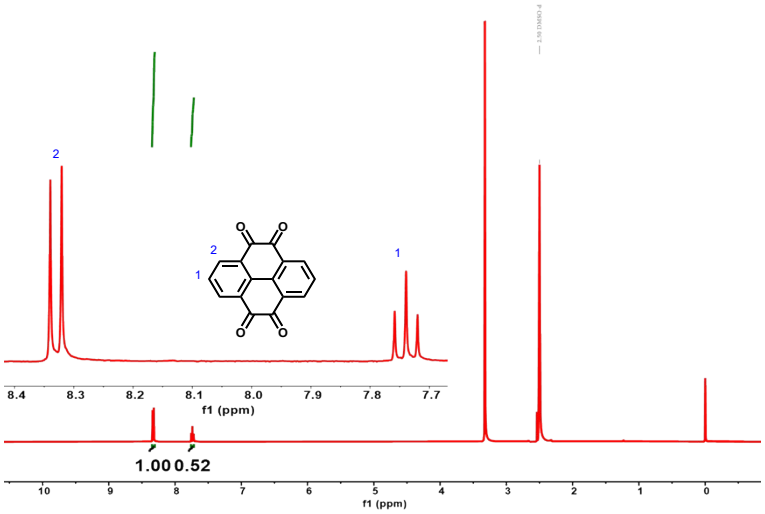

Fig. S1. 1H-NMR spectrum of PT.

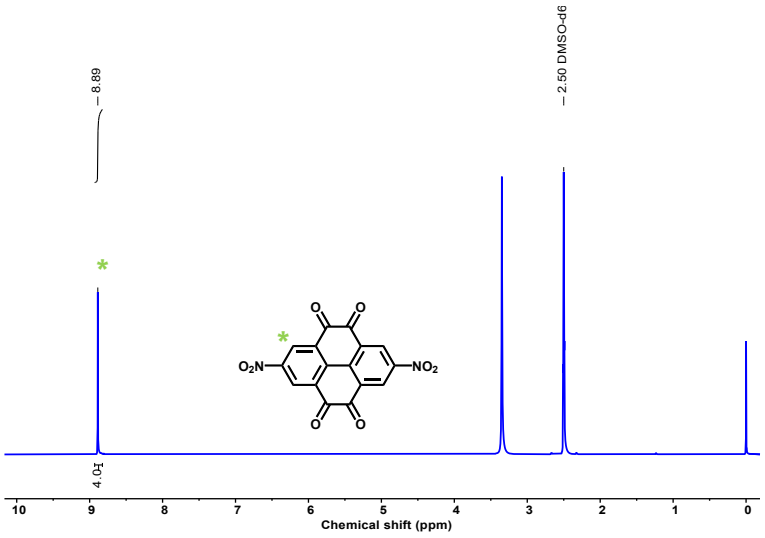

Fig. S2. 1H-NMR spectrum of PT–NO_2.

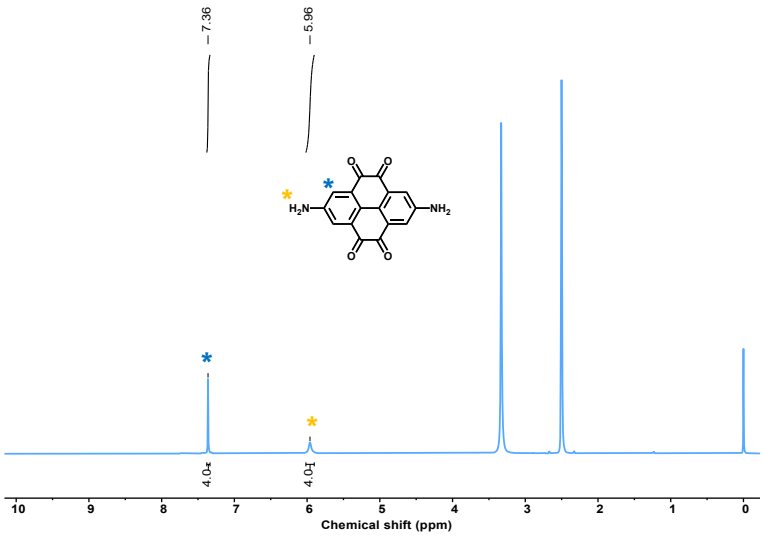

Fig. S3. ^{1}H-NMR spectrum of PT–NH_2.

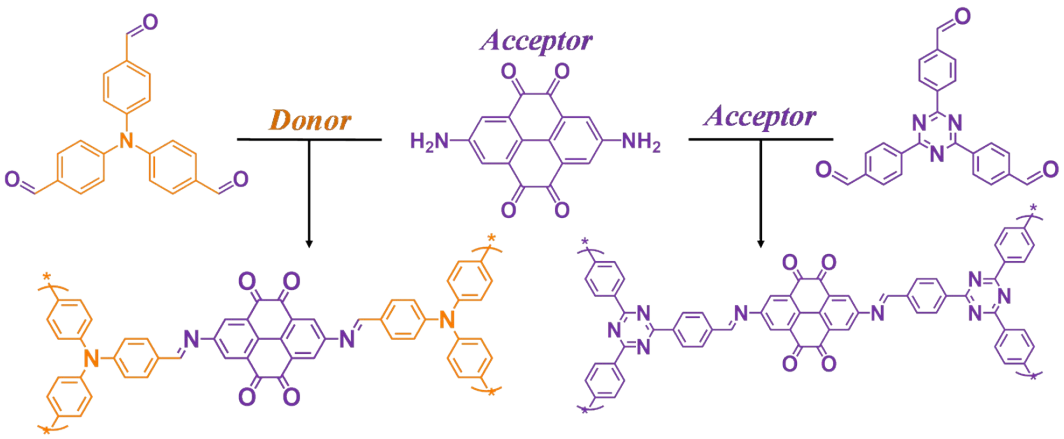

Fig. S4. Schematic illustration of the synthetic routes for PTTA and PTTT.

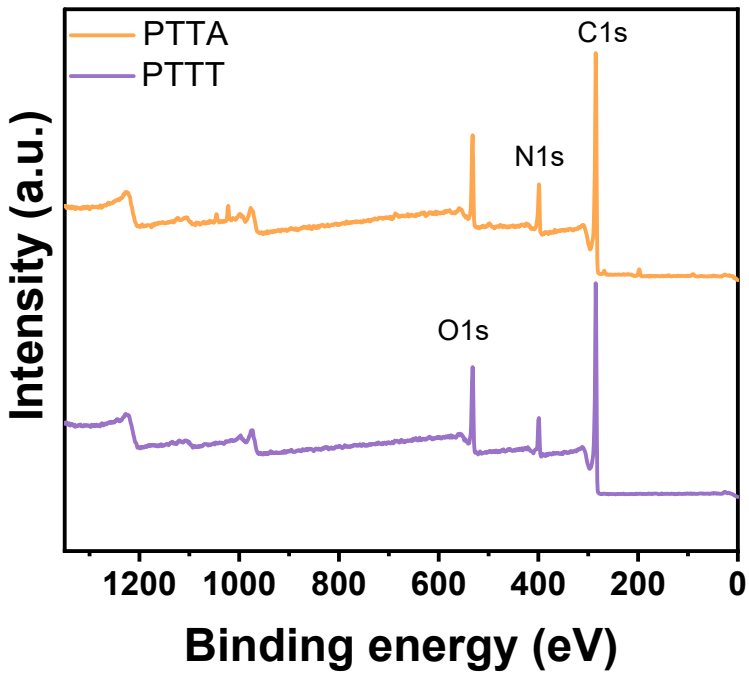

Fig. S5. XPS survey spectrum of PTTA and PTTT.

Survey scan results reveal that PTTT is primarily composed of C, N, and O elements.

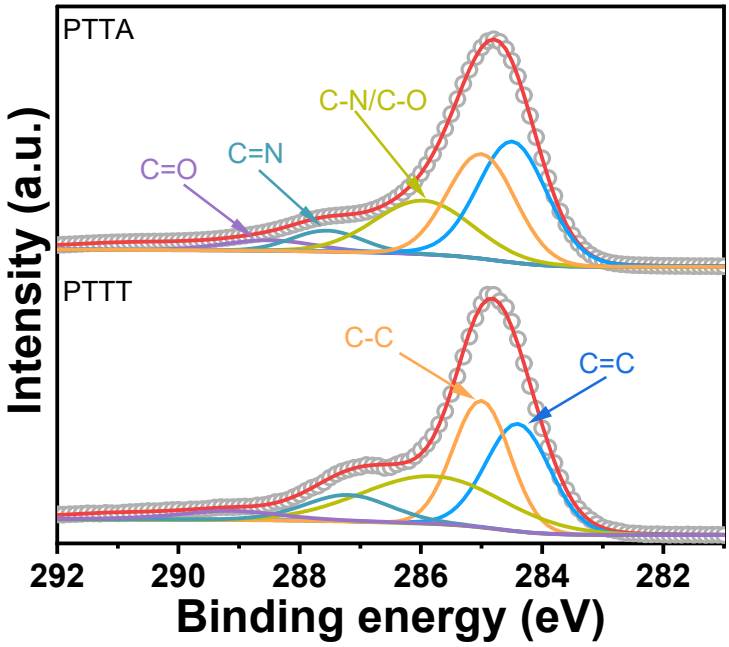

Fig. S6. C1s XPS spectra of PTTA and PTTT.

For PTTT, the C1s spectra exhibits five peaks at 284.5 eV (C=C), 285.0 (C-C), 286.1 eV (C-N), 287.6 eV (C=N), 288.7 eV (C=O) representing the C atoms in benzene ring, imide, triazine, and carbonyl, respectively.

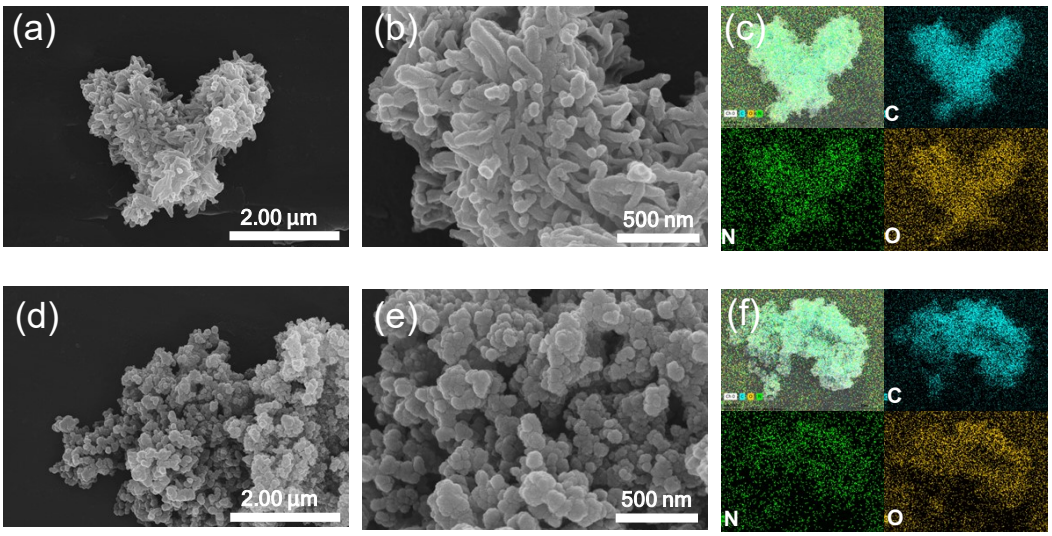

Fig. S7. SEM images of PTTA and PTTT, (a), (b), (c) for PTTA; (d), (e), and (f) for PTTT.

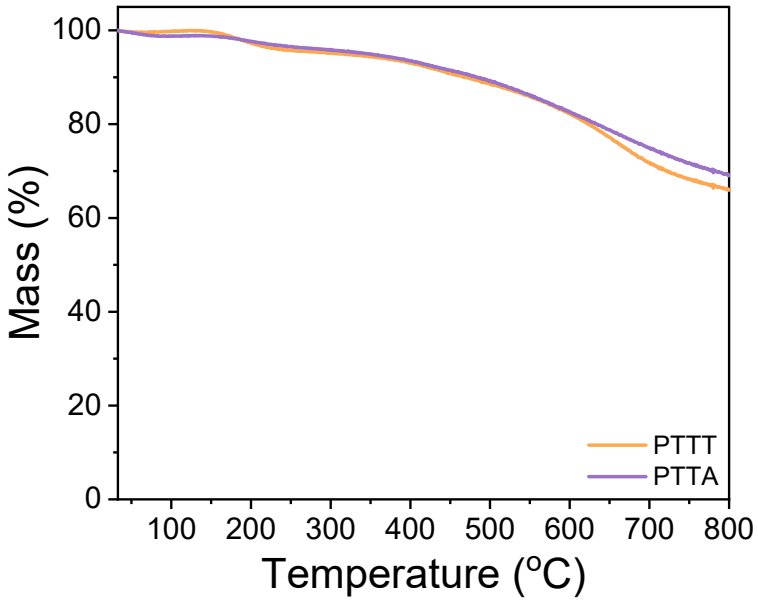

Fig. S8. TGA of PTTA and PTTT.

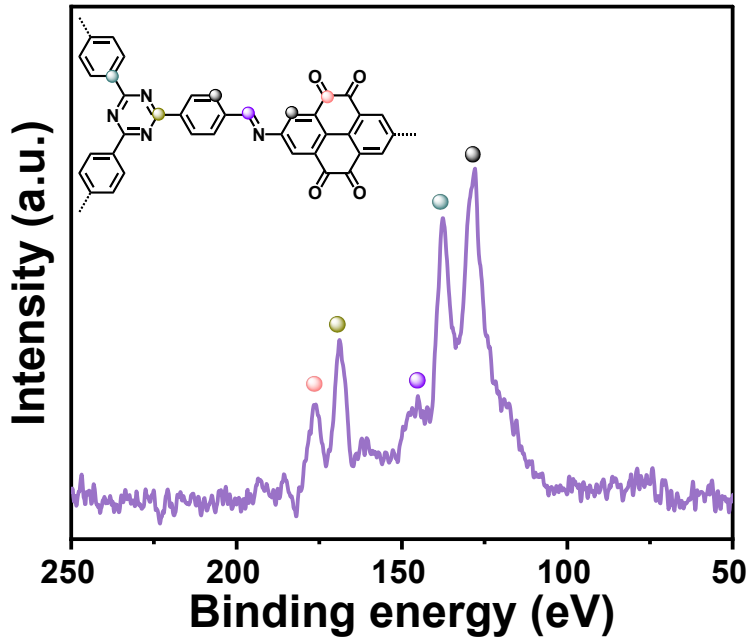

Fig. S9. ^{13}C solid-state NMR spectrum.
Besides, the peaks located at ~169 and ~138 ppm represent the signals for triazine ring in PTTT.

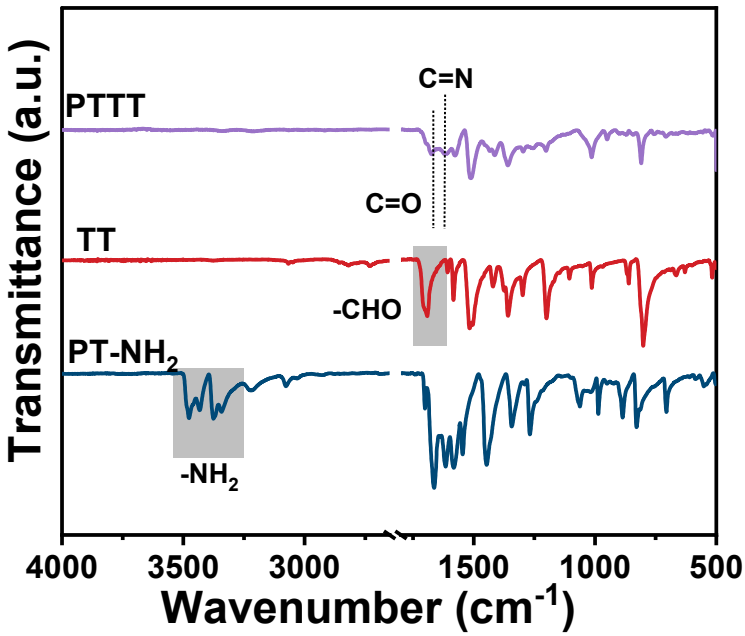

Fig. S10. FT-IR spectra of PTTT

The disappearance of the characteristic –NH_2 stretching vibration peaks (3300–3500 cm^{-1}) in the FTIR spectrum of PTTT confirms the successful occurrence of the Schiff base reaction.

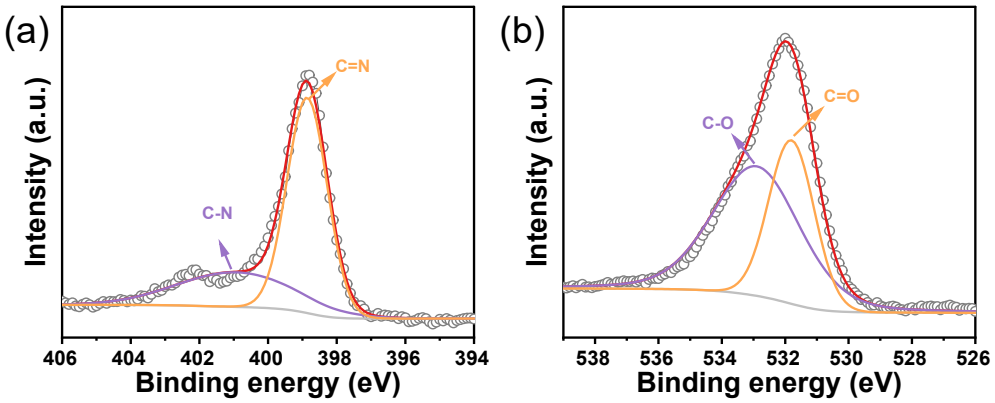

Fig. S11. The O1s and N1s XPS spectra of PTTT.

The peak at 400.1 eV is assigned to C-N bonds within the TA units, while the peak at 399.1 eV corresponds to the C=N bonds of the imine and triazine groups of PTTT. The O1s spectra was resolved into two components, corresponding to C-O (533.3 eV) and C=O (531.6 eV) bonds.

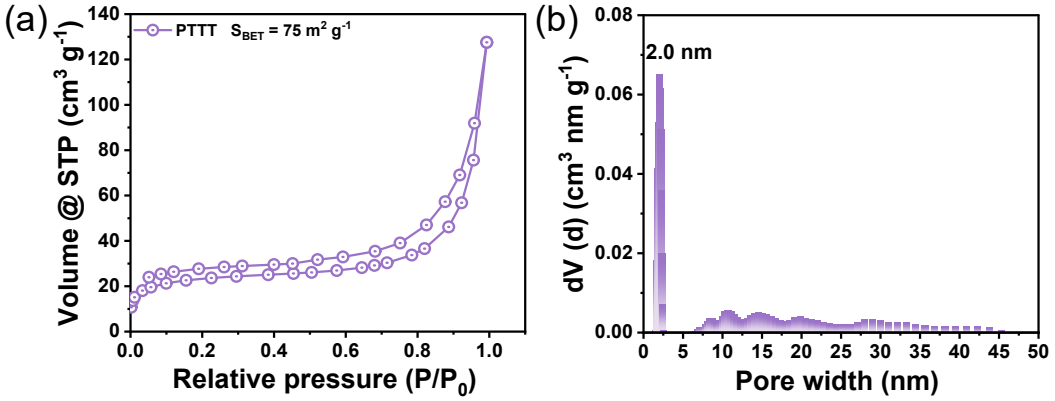

Fig. S12. (a)The N_2 adsorption-desorption isotherms and (b) pore size distribution of PTTT.

The BET surface area of PTTT is 75 m^2 g^{-1}, Its pore size distribution is characterized by dominant micropores centered at ~2 nm, accompanied by mesopores ranging from 5 to 45 nm.

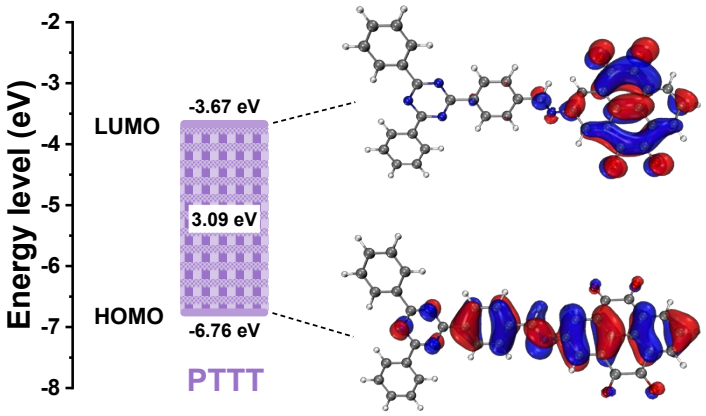

Fig. S13. Calculated energy gap of the PTTT repeating unit and schematic diagram of the LUMO-HOMO molecular orbitals.

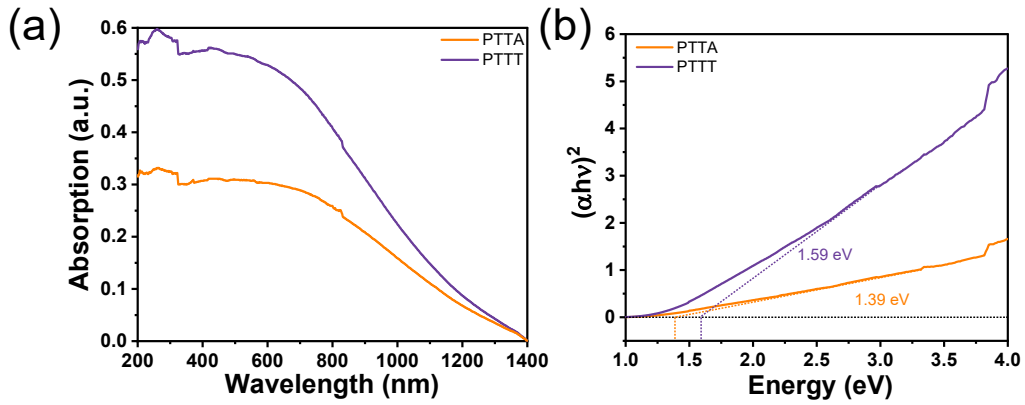

Fig. S14. (a) UV–vis DRS, (b) Tauc plots of PTTA and PTTT.

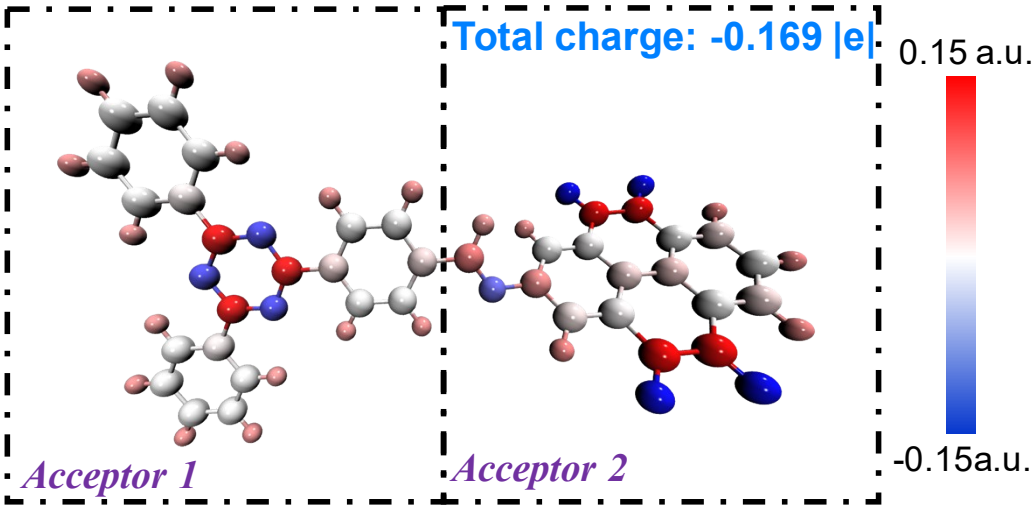

Fig. S15. The Bader charge coloring distribution of PTTT.

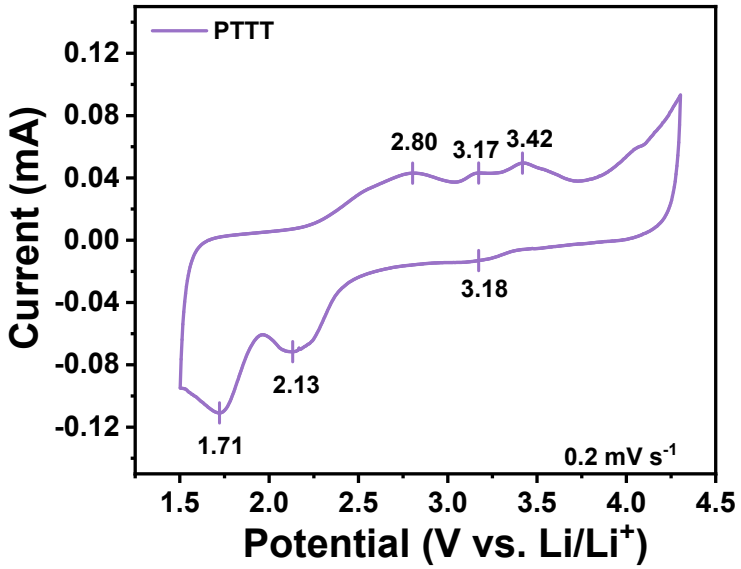

Fig. S16. The CV curve of PTTT at the scan rate of 0.2 mV s^{-1}.

At a scan rate of 0.2 mV s^{-1}, PTTT exhibits three distinct reduction peaks located at 1.7, 2.1, and 3.1 V. When the potential exceeds 3.2 V, only weak electrochemical responses are observed without well-defined redox peaks. In contrast, three oxidation peaks appear at 2.8, 3.2, and 3.4 V, while no obvious redox features are detected in the p-type potential region. These results indicate that the interaction between the triazine units in PTTT and PF_6^- anions in the p-type region is considerably weaker than that of triphenylamine units.

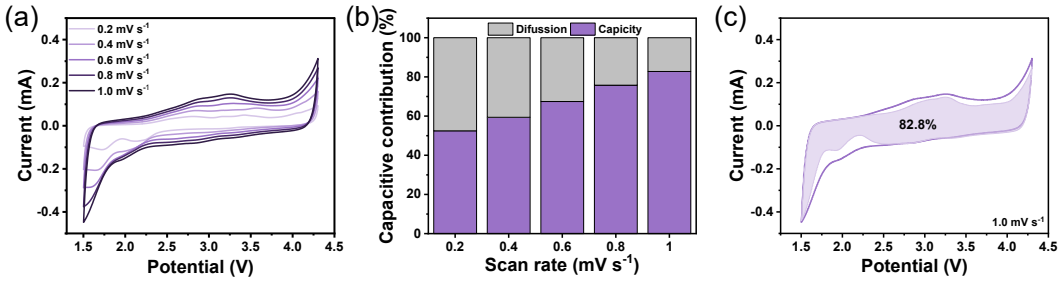

Fig. S17. (a) CV curves at the scan rate of 0.2, 0.4, 0.6, 0.8, 1.0 mV s^{-1}; (b) The capacitive-controlled contribution ratios at different scan rates of PTTT; (c) Capacitive-controlled contribution ratios at 1.0 mV S^{-1}.

The PTTT shows similar trend with PTTA, but the pseudocapacitive contribution ratios are smaller than PTTA. The pseudocapacitive contribution ratio is 52.5% at 0.2 mV s^{-1}, and rises to 82.8% at 1.0 mV s^{-1}.

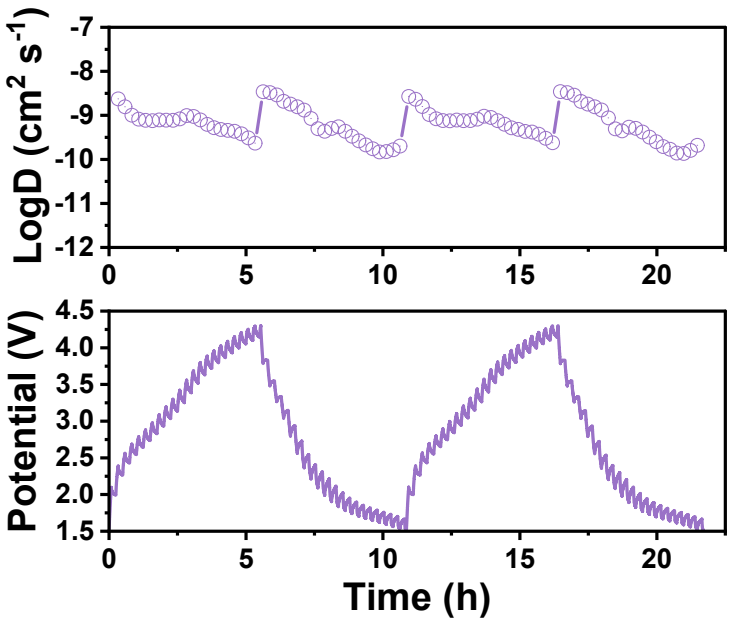

Fig. S18. GITT of PTTT.

The average ion diffusion coefficient of the PTTT electrode is 9.22×10^{-10} cm^2 s^{-1}.

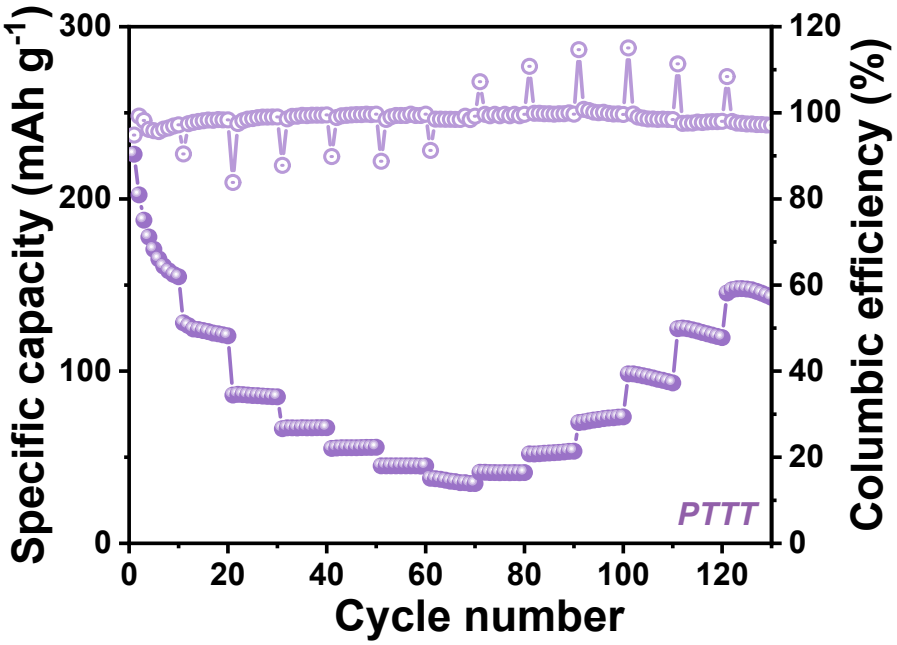

Fig. S19. Rate performance of PTTT cathode at the current densities of 0.1, 0.2, 0.5, 1.0 2.0, 5.0, 10.0 A g^{-1}.

For the PTTT cathode, the capacity is 226 mAh g^{-1} at 0.1 A g^{-1}, whereas it drops sharply to 36 mAh g^{-1} at 10 A g^{-1}. This result highlights the poor rate capability and inferior capacity of PTTT.

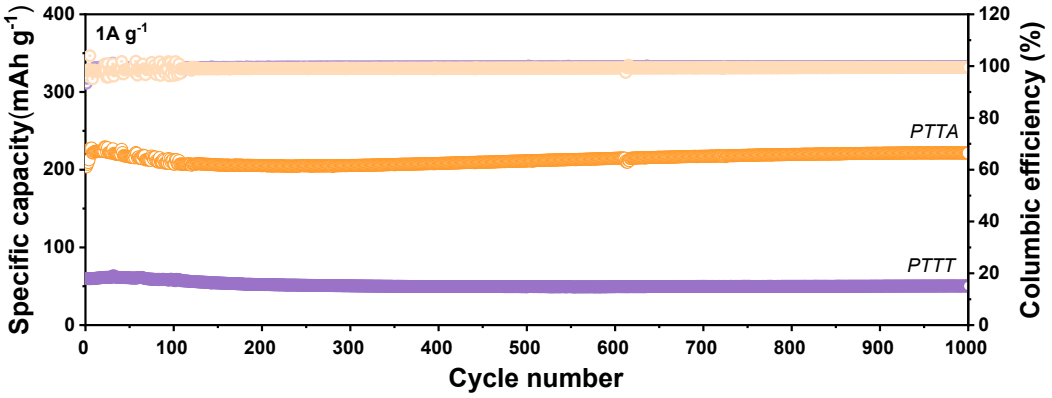

Fig. S20. Cycling performance of PTTA and PTTT at the current density of 1 A g^{-1}.

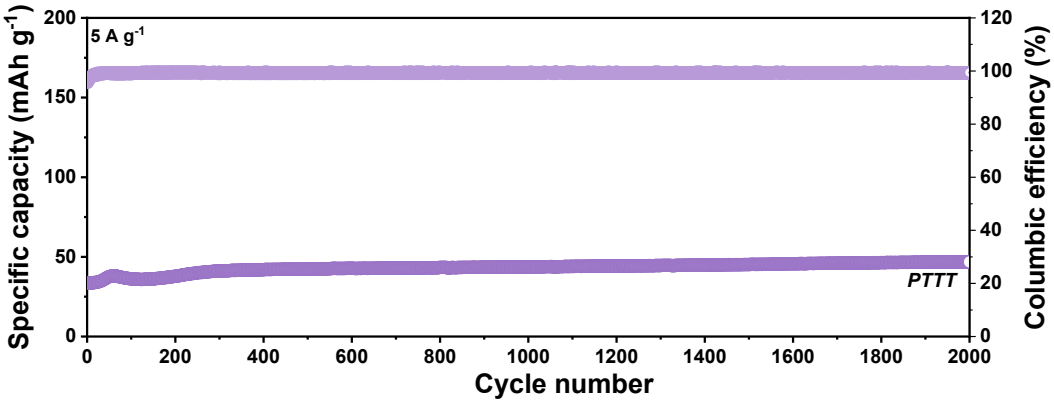

Fig. S21. Cycling performance of PTTT at the current density of 1 A g^{-1}.

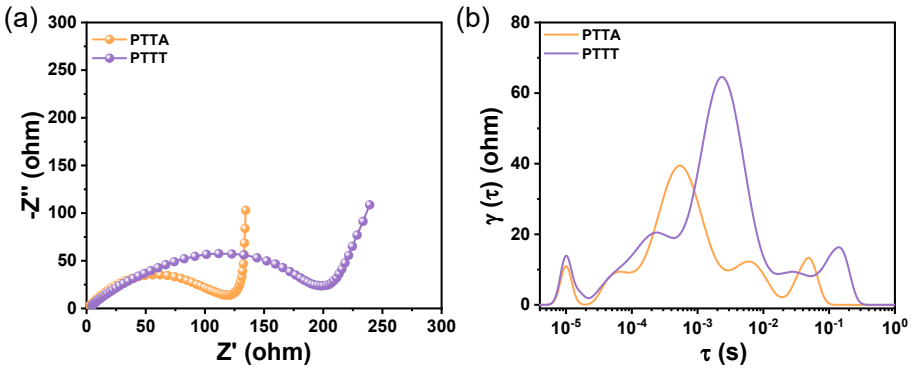

Fig. S22 (a) EIS plots and (b) DRT curves of PTTA and PTTT.

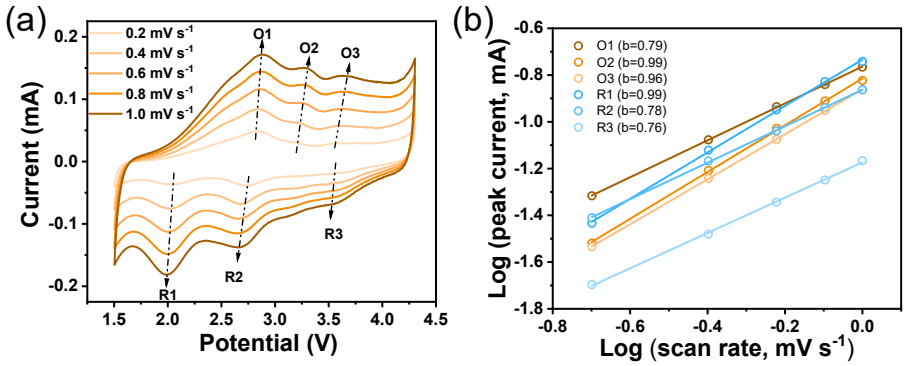

Fig. S23 (a) CV curves of PTTA cathode at the scan rate of 0.2, 0.4, 0.6, 0.8, 1.0 mV s^{-1}; (b) Log (v) versus log (i) plots of PTTA cathode.

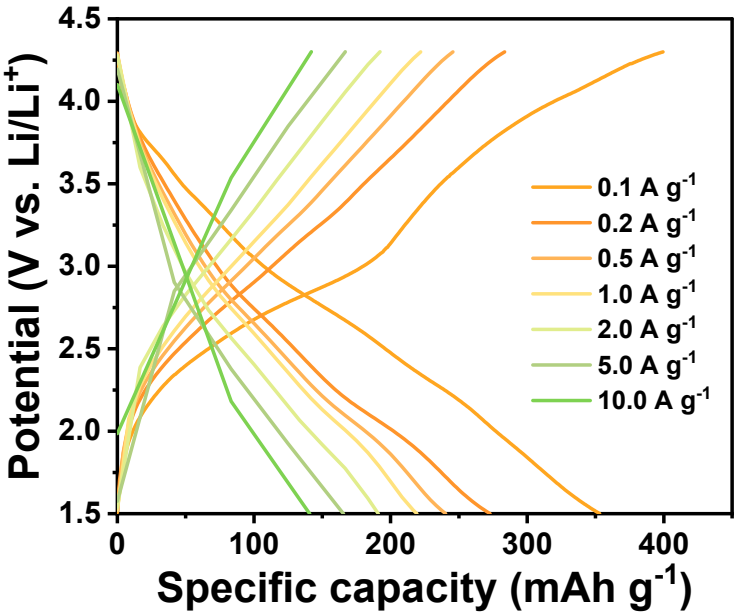

Fig. S24. GCD curves of PTTA at current densities of 0.1, 0.2, 0.5, 1.0 2.0, 5.0, 10.0 A g^{-1}.

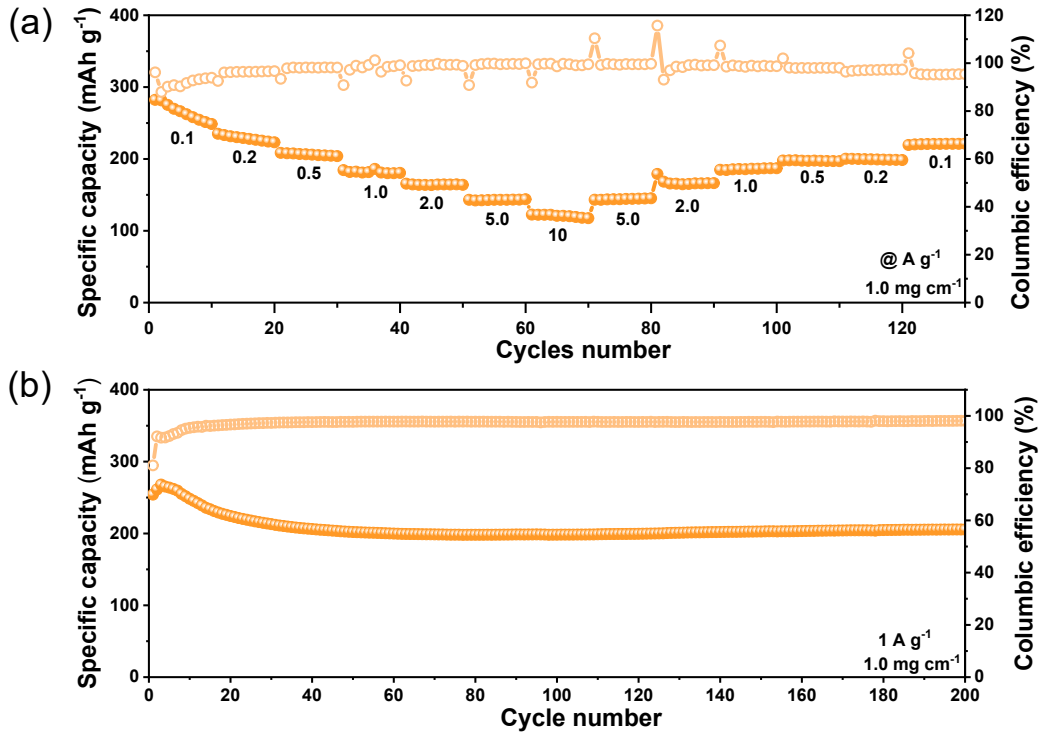

Fig. S25. Rate performance and stability performance of PTTA with a loading mass of 1.0 mg cm^{-2}.

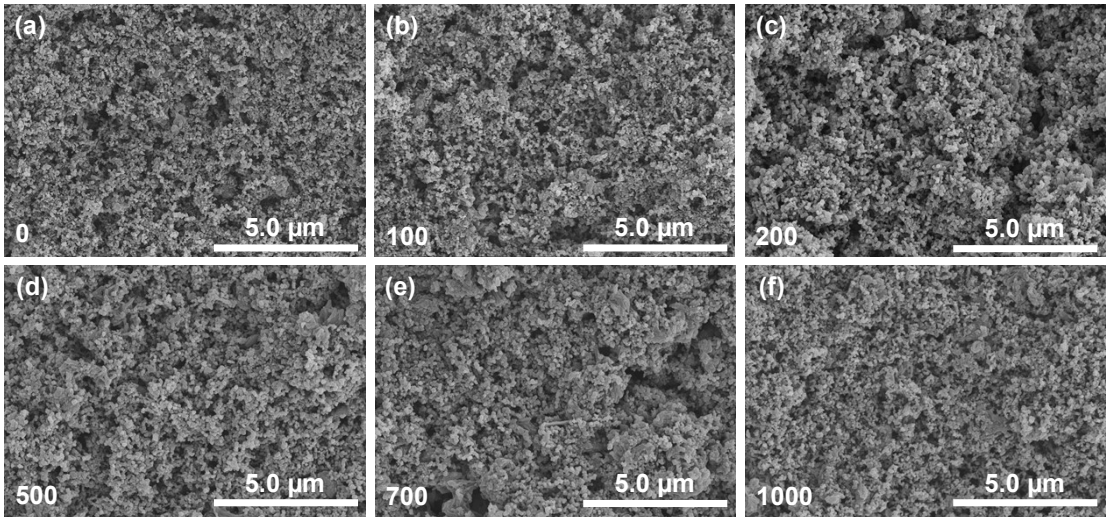

Fig. S26. SEM images of PTTA electrodes after (a) 0 cycle, (b) 100 cycles, (c) 200 cycles, (d) 500 cycles, (e) 700 cycles, and (f) 1000 cycles.

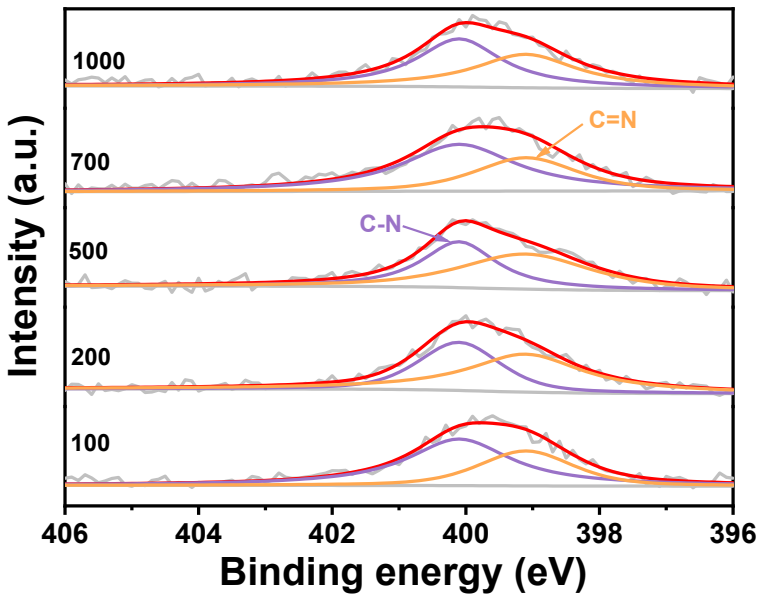

Fig. S27. N1s XPS spectra of PTTA electrodes at different cycles.

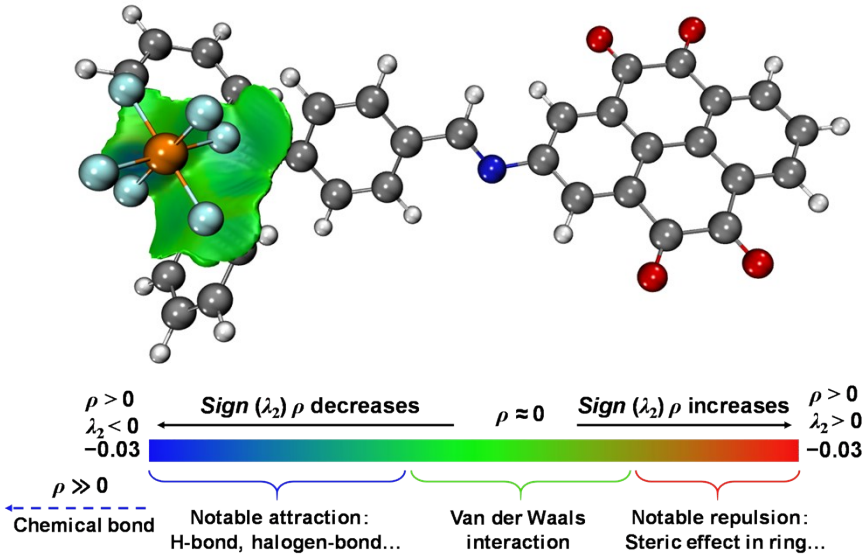

Fig. S28. IGMH analyses between the PF_6^- and PTTA.

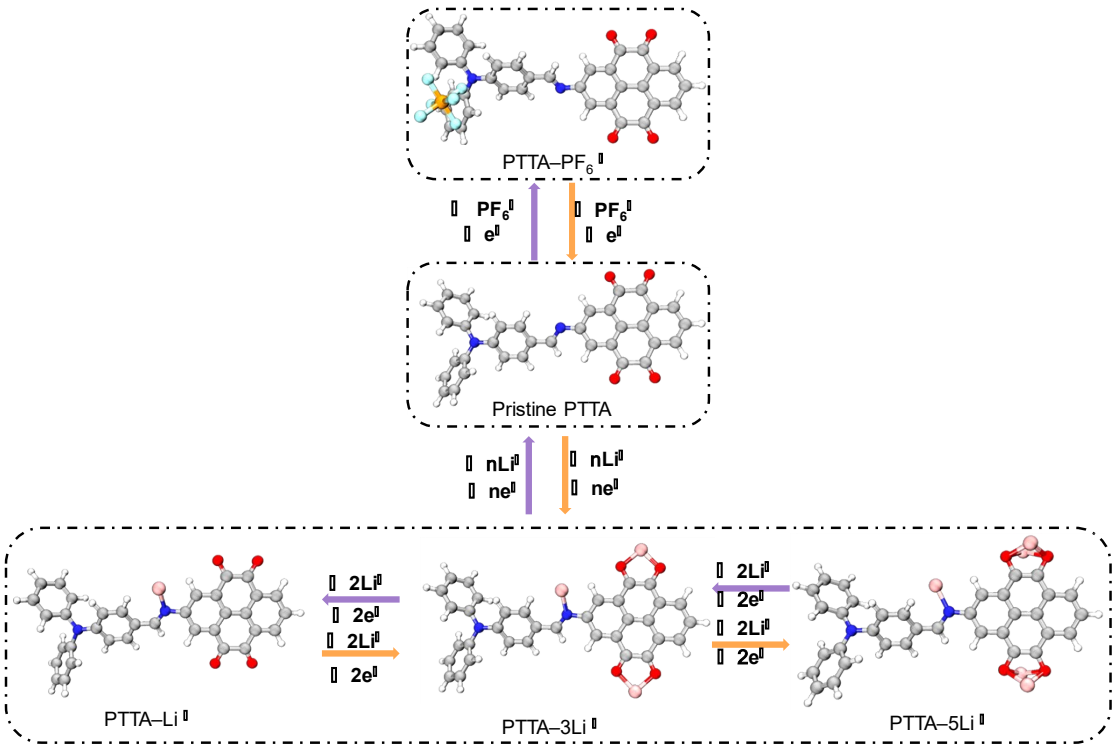

Fig. S29. The electrochemical evolution of PTTA.

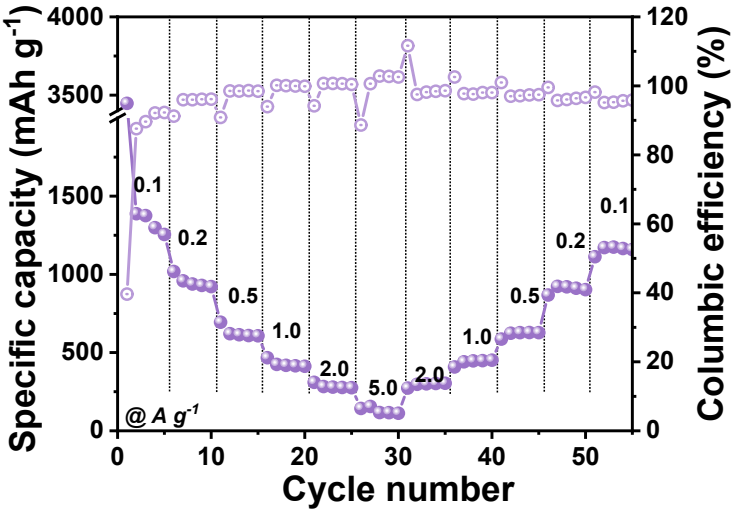

Fig. S30. Rate performance of PTTT anode at current densities of 0.1, 0.2, 0.5, 1.0 2.0, 5.0 A g^{-1}.

For the PTTT anode, the capacity is 1388 mAh g^{-1} at 0.1 A g^{-1}, whereas it drops sharply to 116 mAh g^{-1} at 5 A g^{-1}. This result highlights the poor rate capability and inferior capacity of PTTT.

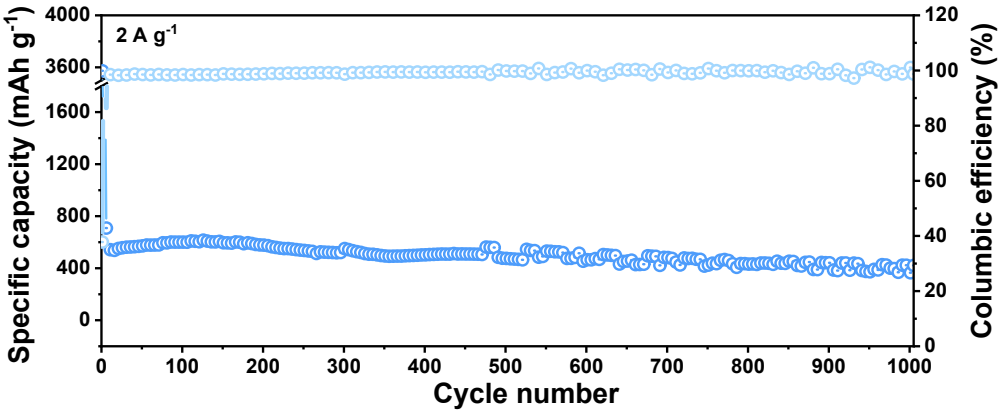

Fig. S31. Cycling performance of PTTA at a current density of 2.0 A g^{-1}.

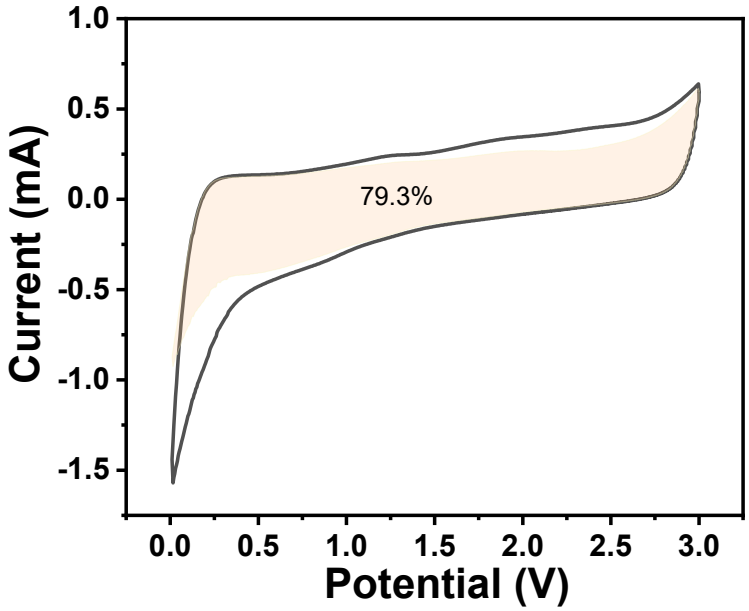

Fig. S32. The capacitive-controlled contribution ratios at 1.0 mV S^{-1} of PTTA.

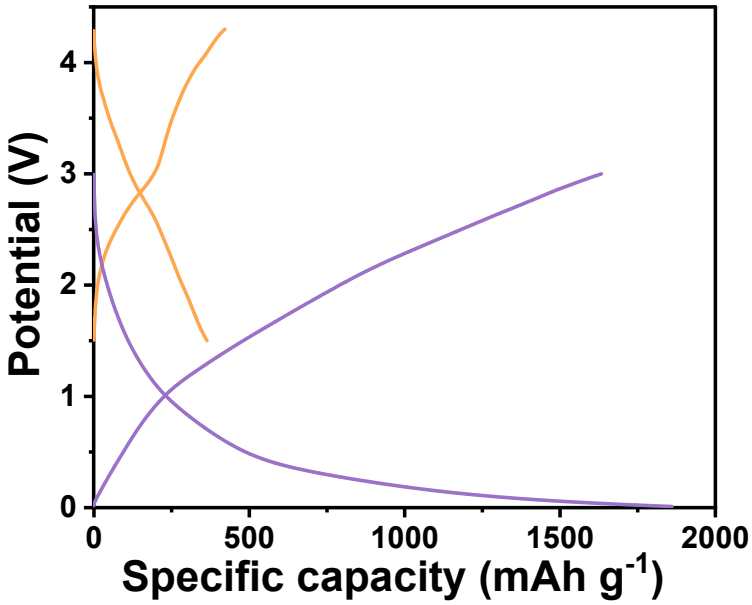

Fig. S33 The discharge curve of PTTA cathode and anode at 0.1 Ag^{-1}

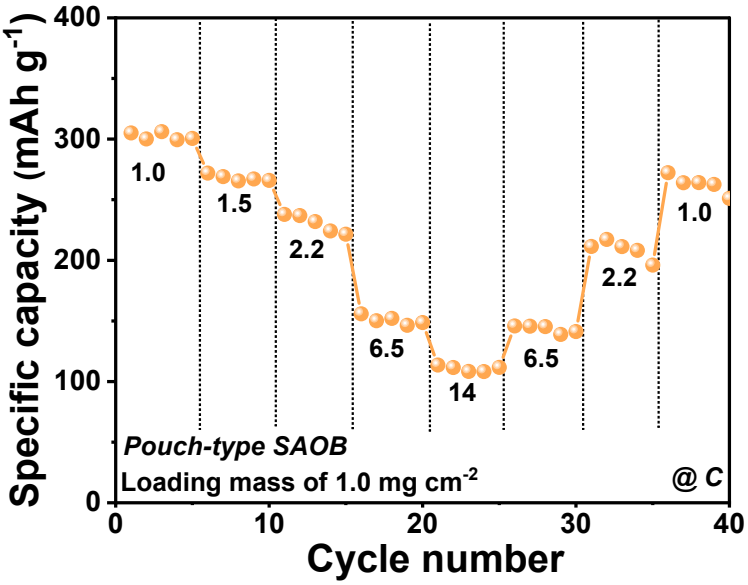

Fig. S34. Rate performance of PTTA-based pouch-type SAOB.

S3.2. Tables

Table S1. Summery and comparison of the rate performances of PTTA and PTTT cathodes at different current densities.

Current density ($A\ g^{-1}$)	Capacity of PTTA cathode ($mAh\ g^{-1}$)	Capacity of PTTT cathode ($mAh\ g^{-1}$)
0.1	353	226
0.2	275	123
0.5	241	85
1.0	220	67
2.0	191	56
5.0	166	45
10.0	142	36

Table S2. Comparison of electrochemical performance with recently reported organic cathodes.

Materials	Specific Capacity ($mAh\ g^{-1}$, $A\ g^{-1}$)	Rate performance ($mAh\ g^{-1}$, $A\ g^{-1}$)	Ref.
TAPT-NTCDA	142/0.05	90/2	10
CuPcNA-CMP	226/0.1	86/5	11
CCP-HATN@CNT	116/0.1	94/1	12
TAPB-NDA@CNT	125/0.025	50/5	13
DAAQ-ECOF	145/0.02	78/3	14
AZO-HATN-AQ	213/0.1	98/8	15
iQCOF	275/0.3	121/10	16
HDA-COF	259/0.05	71/10	17
PTTA	**353/0.1**	**140/10**	**This work**

Table S3. Electrochemical performance comparison of our PTTA based SAOB with recently reported SAOBs.

Note: This study includes both coin-type and pouch-type cells, reference materials are based on coin-type cells only.

Battery	Energy density (Wh kg^{-1})	Power density (W kg^{-1})	Reversible Capacity (mAh g^{-1})/Current density (A g^{-1})	High-rate capacity (mAh g^{-1})/Current density (A g^{-1})	Ref.
PTTA|| PP|| PTTA (Coin-type)	**248**	**10640**	**257/0.3**	**148/10**	**This Work**
PTTA|| PP|| PTTA (pouch-type)	**277**	**1354**	**305/0.3**	**108/5**	**This Work**
TAT-AZO-COF|| PP|| TAT-AZO-COF (Coin-type)	125	9450	210/1	128/10	18
HTPT-COF@CNT|| PP|| HTPT-COF@CNT (Coin-type)	192	3800	257/0.5	216/5	19
CNT@PAQS|| PP|| CNT@CPAN (Coin-type)	86	487	173/0.1	146/1	20
CNT@PMAQ|| PP|| CNT@PMAQ (Coin-type)	315	1801	235/0.02	58/1	21
TAPT|| PP|| TAPT (Coin-type)	147	322	361/0.1	217/1	22
Ni-TABQ|| PP|| Ni-TABQ	142	5160	169/0.05	41.7/5	23

(Coin-type)					
PZDB-Li_2|| PP|| PZDB-Li_2 (Coin-type)	132	617	54/0.0617	45/0.25	24
PDB|| PP|| PDB (Coin-type)	276	948	249/0.02	55/1	25

S4. Supplementary references

1. S. Zheng, D. Shi, T. Sun, L. Zhang, W. Zhang, Y. Li, Z. Guo, Z. Tao and J. Chen, *Angew. Chem. Int. Ed.*, 2023, **62**, e202217710.

2. M. J. Frisch, G. W. Trucks, H. B. Schlegel, G. E. Scuseria, M. A. Robb, J. R. Cheeseman, G. Scalmani, V. Barone, G. A. Petersson, H. Nakatsuji, X. Li, M. Caricato, A. V. Marenich, J. Bloino, B. G. Janesko, R. Gomperts, B. Mennucci, H. P. Hratchian, J. V. Ortiz, A. F. Izmaylov, J. L. Sonnenberg, Williams, F. Ding, F. Lipparini, F. Egidi, J. Goings, B. Peng, A. Petrone, T. Henderson, D. Ranasinghe, V. G. Zakrzewski, J. Gao, N. Rega, G. Zheng, W. Liang, M. Hada, M. Ehara, K. Toyota, R. Fukuda, J. Hasegawa, M. Ishida, T. Nakajima, Y. Honda, O. Kitao, H. Nakai, T. Vreven, K. Throssell, J. A. Montgomery Jr., J. E. Peralta, F. Ogliaro, M. J. Bearpark, J. J. Heyd, E. N. Brothers, K. N. Kudin, V. N. Staroverov, T. A. Keith, R. Kobayashi, J. Normand, K. Raghavachari, A. P. Rendell, J. C. Burant, S. S. Iyengar, J. Tomasi, M. Cossi, J. M. Millam, M. Klene, C. Adamo, R. Cammi, J. W. Ochterski, R. L. Martin, K. Morokuma, O. Farkas, J. B. Foresman and D. J. Fox, *Journal*, 2016.

3. A. D. Becke, *The Journal of Chemical Physics*, 1993, **98**, 5648-5652.

4. W. J. Hehre, R. Ditchfield and J. A. Pople, *The Journal of Chemical Physics*, 1972, **56**, 2257-2261.

5. S. Grimme, J. Antony, S. Ehrlich and H. Krieg, *The Journal of Chemical Physics*, 2010, **132**.

6. F. Weigend and R. Ahlrichs, *Phys. Chem. Chem. Phys.*, 2005, **7**, 3297-3305.

7. T. Lu and F. Chen, *J. Comput. Chem.*, 2012, **33**, 580-592.

8. W. Humphrey, A. Dalke and K. Schulten, *J. Mol. Graph.*, 1996, **14**, 33-38.

9. A. Singh, P. Bhauriyal, L. Quincke, D. Blätte, R. Guntermann, J. L. Rupp, T. Heine and T. Bein, *Adv. Energy Mater.*, 2025, **15**, e01494.

10. K. Li, Y. Wang, B. Gao, X. Lv, Z. Si and H.-g. Wang, *J. Colloid Interface Sci.*, 2021, **601**, 446-453.

11. H.-g. Wang, Q. Li, Q. Wu, Z. Si, X. Lv, X. Liang, H. Wang, L. Sun, W. Shi and S. Song, *Adv. Energy Mater.*, 2021, **11**, 2100381.

12. S. Xu, G. Wang, B. P. Biswal, M. Addicoat, S. Paasch, W. Sheng, X. Zhuang, E. Brunner, T. Heine, R. Berger and X. Feng, *Angew. Chem. Int. Ed.*, 2019, **58**, 849-853.

13. S. Biswas, A. Pramanik, A. Dey, S. Chattopadhyay, T. S. Pieshkov, S. Bhattacharyya, P. M. Ajayan and T. K. Maji, *Small*, 2024, **20**, 2406173.

14. S. Wang, Q. Wang, P. Shao, Y. Han, X. Gao, L. Ma, S. Yuan, X. Ma, J. Zhou, X. Feng and B. Wang, *J. Am. Chem. Soc.*, 2017, **139**, 4258-4261.

15. Z. Sun, H. Yao, J. Li, B. Liu, Z. Lin, M. Shu, H. Liu, S. Zhu and S. Guan, *ACS Appl. Mater. Interfaces*, 2023, **15**, 42603-42610.

16. J. Duan, F. Chen, H. Yu, S. Zhu, L. Teng, K. Wang, T. Chen, W. Lyu, H. Hu and Y. Liao, *Angew. Chem. Int. Ed.*, 2025, **64**, e202505207.

17. J. Duan, L. Teng, H. Liu, X. Zhang, H. Yu, Q. Huang, Y. Li, M. Liu, H. Hu, W. Lyu and Y. Liao, *Angew. Chem. Int. Ed.*, 2025, **64**, e202517853.

18. W. Feng, Z. Yang, C. Guo, H. Zhuang, R. Xu, H. Zhang, M. Shi, Z. Chen, Y. Chen and Y.-Q. Lan, *Angew. Chem. Int. Ed.*, 2025, **64**, e202508937.

19. Y. Wang, J. Wang, J. Peng, Y. Jiang, Y. Zhu and Y. Yang, *ACS Nano*, 2024, **18**, 23958-23967.

20. Y. Wang, K. Chen, Y. Zhu, J. Wang, N. Jiang and Y. Yang, *Energy Environ. Mater.*, 2023, **6**, e12564.

21. Q. Zhang, Y. He, Y. Wang, J. Lu, N. Jiang and Y. Yang, *Adv. Funct. Mater.*, 2023, **33**, 2211590.
22. Z. Li, Q. Jia, Y. Chen, K. Fan, C. Zhang, G. Zhang, M. Xu, M. Mao, J. Ma, W. Hu and C. Wang, *Angew. Chem. Int. Ed.*, 2022, **61**, e202207221.
23. K. Li, J. Yu, Z. Si, B. Gao, H.-g. Wang and Y. Wang, *Chem. Eng. J.*, 2022, **450**, 138052.
24. G. Dai, Y. He, Z. Niu, P. He, C. Zhang, Y. Zhao, X. Zhang and H. Zhou, *Angew. Chem. Int. Ed.*, 2019, **58**, 9902-9906.
25. J. Xie, Z. Wang, Z. J. Xu and Q. Zhang, *Adv. Energy Mater.*, 2018, **8**, 1703509.